

Calculation of Debye-Scherrer diffraction patterns from highly stressed polycrystalline materials

M. J. MacDonald,^{1,2,*} J. Vorberger,³ E. J. Gamboa,² R. P. Drake,⁴ S. H. Glenzer,² and L. B. Fletcher²

¹*Applied Physics Program, University of Michigan, Ann Arbor, Michigan 48109, USA*

²*SLAC National Accelerator Laboratory, Menlo Park, California 94025, USA*

³*Helmholtz Zentrum Dresden-Rossendorf, 01328 Dresden, Germany*

⁴*Climate and Space Sciences and Engineering, Applied Physics,
and Physics, University of Michigan, Ann Arbor, Michigan 48109, USA*

(Dated: May 19, 2016)

Calculations of Debye-Scherrer diffraction patterns from polycrystalline materials have typically been done in the limit of small deviatoric stresses. Although these methods are well suited for experiments conducted near hydrostatic conditions, more robust models are required to diagnose the large strain anisotropies present in dynamic compression experiments. A method to predict Debye-Scherrer diffraction patterns for arbitrary strains has been presented in the Voigt (iso-strain) limit [A. Higginbotham, J. Appl. Phys. **115**, 174906 (2014)]. Here we present a method to calculate Debye-Scherrer diffraction patterns from highly stressed polycrystalline samples in the Reuss (iso-stress) limit. This analysis uses elastic constants to calculate lattice strains for all initial crystallite orientations, enabling elastic anisotropy and sample texture effects to be modeled directly. The effects of probing geometry, deviatoric stresses, and sample texture are demonstrated and compared to Voigt limit predictions. An example of shock-compressed polycrystalline diamond is presented to illustrate how this model can be applied and demonstrates the importance of including material strength when interpreting diffraction in dynamic compression experiments.

I. INTRODUCTION

The behavior of materials under dynamic compression is of interest to several fields including the modeling of planetary interiors and meteor impact events,¹ exploring high pressure phase changes,^{2–4} and understanding the initial compression phase of inertial confinement fusion implosions.^{5,6} Accurate measurements of the strength of materials at high strain rate is critical in predicting their response to the dynamic loading conditions present in these studies. X-ray diffraction provides a powerful technique for probing the structure of crystalline materials and can be used to directly measure lattice strains and material strength.

Free electron lasers (FELs), such as the Linac Coherent Light Source, enable compressed states to be probed with high peak brightness and ~ 40 fs time resolution.^{7,8} The pulse duration of these x-ray pulses is shorter than the smallest phonon period in shocked systems, allowing lattice dynamics to be studied without temporal smearing. FELs produce nearly monochromatic x-rays, requiring polycrystalline samples to produce Debye-Scherrer diffraction rings from a compressed lattice.

By varying the pressure source, dynamic compression experiments can access a wide range of pressure-density space. These include accessing Hugoniot states via shock compression^{8–19} as well as off-Hugoniot states using ramp laser drive pulses,^{20–22} pulsed-power devices,^{23–25} or laser-driven plasma loaders.^{26,27} Additionally, large-scale laser facilities have recently demonstrated the ability to study material properties of dynamically compressed solids up to five TPa.²¹ Analyzing diffraction data from crystalline materials at such high pressures requires a method capable of predicting diffraction beyond

the small-strain limit.

Analytical models of the stress-strain relationship for polycrystalline materials require assumptions on the behavior at the grain boundaries. The Voigt limit²⁸ assumes strain is continuous across grain boundaries while the Reuss limit²⁹ assumes continuous stress. Diffraction from compressed crystalline materials has commonly been analyzed using a method originally presented by Singh³⁰ in the small-strain limit. For the highly strained conditions present in dynamic compression experiments, a method to model diffraction in the Voigt limit has been presented,³¹ but no method in the Reuss limit has been published.

A Reuss limit model would be particularly important for polycrystalline materials with elastic anisotropy, which have directionally-dependent stress-strain relationships. In these cases, a distribution of strain states would be expected to be present for a nonhydrostatic stress applied to the sample. This behavior is not included in Voigt limit models, which assume that the same strain tensor is applied to all crystallites, regardless of orientation within the sample.

Here, we present a method to calculate the diffraction pattern and lattice strains polycrystalline samples in the Reuss limit for highly stressed materials. This method takes the set of all initial crystallite orientations, defined by the initial texture of the sample, and applies the transformed stress tensor to each orientation before calculating the resulting diffraction pattern. With this method, we fit the applied stress tensor to diffraction data, enabling direct comparison to pressures measured experimentally or calculated using equation-of-state models. We present examples illustrating how probing geometry, deviatoric stresses, and sample texture affect Debye-

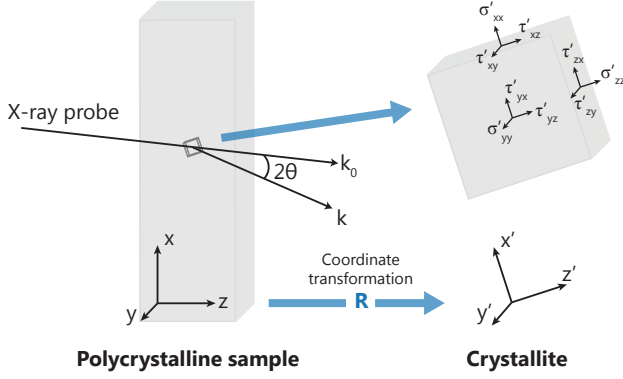


FIG. 1. (color) Definition of the coordinate systems used in this paper. The laboratory frame is unprimed and the coordinate system of the crystal lattice for a given crystallite within the sample is primed. The x-ray probe and diffracted wave vectors are \mathbf{k}_0 and \mathbf{k} and the angle between them is defined as 2θ . The stress directions for the Cauchy stress tensor in the crystallite coordinate system, where shear stresses are nonzero after transformation from the laboratory frame, are also shown.

Scherrer diffraction patterns. Finally, we show an example of diffraction from shock compressed polycrystalline diamond using elastic constants calculated using density functional theory (DFT) combined with pressure calculations from Rankine-Hugoniot equations to demonstrate how the technique can be applied.

II. APPLICATION OF THE STRESS FIELD

The critical component of the method presented here is the proper application of the stress tensor to a polycrystalline material. This requires the stress tensor, which is defined in the laboratory frame, to be applied to each crystallite within the sample by transforming the tensor into the frame of each crystallite. We define three coordinate systems: the unprimed laboratory frame coordinates and the primed crystal lattice coordinate system as shown in Fig. 1, as well as a diffraction coordinate system denoted by double primes described in the diffraction calculation section.

The applied stress tensor is defined in the laboratory frame by the Cauchy stress tensor, which includes compressive and shear stresses. It is defined as

$$\sigma = \begin{pmatrix} \sigma_x & \tau_{xy} & \tau_{xz} \\ \tau_{yx} & \sigma_y & \tau_{yz} \\ \tau_{zx} & \tau_{zy} & \sigma_z \end{pmatrix}, \quad (1)$$

where σ_i is a compressive stress in the i direction and τ_{ij} is a shear stress applied to the i face in the j direction. These stresses are illustrated in the crystallite coordinate system in Fig. 1.

Transforming the stress tensor from the laboratory frame to the crystallite frame is required to correctly predict the lattice strains for materials with elastic anisotropy and enables the use of elastic constants to calculate lattice strains. The tensor is transformed by applying a rotation to the stress in the lab frame using a rotation matrix, \mathbf{R} , defined between the two frames. The Cauchy stress tensor is transformed between coordinate systems by

$$\sigma' = \mathbf{R}\sigma\mathbf{R}^T. \quad (2)$$

The rotation matrix is chosen to use proper Euler angles using a z - y - z rotation,

$$\mathbf{R}(\alpha, \beta, \gamma) = \mathbf{R}_z(\gamma)\mathbf{R}_y(\beta)\mathbf{R}_z(\alpha), \quad (3)$$

where R_y and R_z are the standard rotation matrices about the y and z axes,

$$\mathbf{R}_y(\phi) = \begin{pmatrix} \cos \phi & 0 & \sin \phi \\ 0 & 1 & 0 \\ -\sin \phi & 0 & \cos \phi \end{pmatrix} \quad (4)$$

and

$$\mathbf{R}_z(\phi) = \begin{pmatrix} \cos \phi & -\sin \phi & 0 \\ \sin \phi & \cos \phi & 0 \\ 0 & 0 & 1 \end{pmatrix}. \quad (5)$$

where the angles between the coordinate systems depend on the orientation of each crystallite.

Calculating the lattice strains created by the stress tensor in the crystallite frame requires knowledge of the stress-strain relationship for the material. In principle, if this relationship is known for all stress states (including for all rotations) this method can be used to calculate the diffraction patterns for any stress. In practice, the stress-strain relationship is only known for specific conditions. In this paper we assume that the stress-strain relationship for the material is known under hydrostatic compression, and elastic constants are used to calculate lattice strains for deviatoric stresses.

III. DIFFRACTION CALCULATION

For each compressed crystallite, the Laue diffraction condition can be used to determine which crystal planes will contribute to the diffraction signal. This analysis is done in reciprocal space, where the reciprocal lattice vectors are calculated by the following:

$$\mathbf{a}^* = \frac{2\pi}{V} \mathbf{b}' \times \mathbf{c}' \quad (6)$$

$$\mathbf{b}^* = \frac{2\pi}{V} \mathbf{c}' \times \mathbf{a}' \quad (7)$$

$$\mathbf{c}^* = \frac{2\pi}{V} \mathbf{a}' \times \mathbf{b}', \quad (8)$$

where \mathbf{a}' , \mathbf{b}' , and \mathbf{c}' are crystal lattice vectors in real space and V is the volume of the unit cell. The reciprocal lattice vector for a crystal plane with Miller indices (hkl) is defined as $\mathbf{G}' = h\mathbf{a}^* + k\mathbf{b}^* + l\mathbf{c}^*$ and d spacing of the crystal plane is given by $d = 2\pi/G'$.

The condition for Bragg scattering for a crystal plane with spacing d is given by $n\lambda = 2d \sin \theta_B$, where n is the diffraction order, λ is the x-ray wavelength, and θ_B is the Bragg angle. The Laue diffraction condition is given in the laboratory frame by $\mathbf{k} - \mathbf{k}_0 = \mathbf{G}$, where \mathbf{k}_0 and \mathbf{k} are the probe and scattered x-ray wave vectors, respectively. The magnitude of the probe wave vector is given by $k_0 = 2\pi/\lambda$ and x-ray diffraction is an elastic scattering process, so we can assume $|\mathbf{k}_0| = |\mathbf{k}|$. By transforming \mathbf{G}' to the laboratory frame ($\mathbf{G} = \mathbf{R}^T \cdot \mathbf{G}'$) and using these conditions, the scattering intensity from a plane can be evaluated by calculating $\Delta\theta_B$, the deviation from the ideal Bragg angle, given by

$$\Delta\theta_B = \arcsin\left(n \frac{G}{2k_0}\right) + \arcsin\left(n \frac{\mathbf{k}_0 \cdot \mathbf{G}}{k_0 G}\right), \quad (9)$$

and sampling the rocking curve of the material at this value. The spectral bandwidth and divergence of the probe source can be modeled in this step by sampling a distribution of \mathbf{k}_0 vectors.

Diffraction patterns can be visualized by plotting the diffracted rays on a plane normal to the \mathbf{k}_0 with coordinates denoted by double primes. Scattered wavevectors, \mathbf{k} , transformed into this frame are used to calculate the angular position around the diffraction ring, given by $\phi = \arctan(k_y''/k_x'')$. The diffraction pattern is converted by Cartesian coordinates using

$$x''/L = \tan 2\theta \cos \phi \quad (10)$$

$$y''/L = \tan 2\theta \sin \phi \quad (11)$$

where L is the distance between the sample and the $(xy)''$ plane. For the compressed crystallites contributing to the diffraction pattern, the lattice strains, diffraction angles, and diffracted intensities can be recorded.

IV. UNIAXIAL COMPRESSION

Uniaxial compression is a common way to study materials at high pressure and is relevant to both diamond anvil cell and dynamic compression experiments. In

uniaxial compression, off-diagonal stress tensor components in the laboratory frame can be disregarded and the Cauchy stress tensor can be decomposed into two components: a hydrostatic component and a traceless deviatoric component. The hydrostatic component provides the mean stress and the deviatoric component allows additional stress to be applied in the direction of compression. The decomposed stress tensor in the laboratory frame can thus be written³⁰

$$\sigma = \sigma_{\mathbf{h}} + \sigma_{\mathbf{d}} = \begin{pmatrix} \sigma_h & 0 & 0 \\ 0 & \sigma_h & 0 \\ 0 & 0 & \sigma_h \end{pmatrix} + \begin{pmatrix} -t/3 & 0 & 0 \\ 0 & -t/3 & 0 \\ 0 & 0 & 2t/3 \end{pmatrix}, \quad (12)$$

where $\sigma_{\mathbf{h}}$ and $\sigma_{\mathbf{d}}$ are the hydrostatic and deviatoric stress tensors and t is the uniaxial stress component.

The compression of the crystallites is calculated in two steps. First, the hydrostatic stress component is applied to all crystallites, scaling the crystal lattice by the compression calculated using a hydrostatic compression curve, which does not depend on crystallite orientation. For this step, each crystal lattice vector transforms as

$$\mathbf{v}'_h = \frac{\rho_0}{\rho_h} \mathbf{v}'_0, \quad (13)$$

where $\mathbf{v}_{\mathbf{h}}$ and \mathbf{v}_0 are the hydrostatically compressed and uncompressed lattice vectors and ρ_h and ρ_0 are the hydrostatically compressed and initial densities. For high pressure conditions or materials with low strength this will provide the majority of the compression of the crystal lattice. It is important to do this step before applying the deviatoric component, which requires the use of elastic constants and therefore should be treated as a perturbation on the compressed cell to minimize error.

Next, the deviatoric component is calculated by applying the elastic constants, which are calculated using DFT as a function of hydrostatic pressure, to the compressed cell. For a linear system, the lattice strains are calculated using

$$\sigma'_d = \mathbf{C} \epsilon'_d \quad (14)$$

where ϵ'_d is the deviatoric strain tensor and \mathbf{C} is the elastic stiffness tensor. For high-strength materials the deviatoric strains can be large and higher order elastic constants may be needed to properly model the system.

The strain tensor is applied to each crystal lattice vector in the hydrostatically compressed system by

$$\mathbf{v}' = \begin{pmatrix} 1 + \epsilon'_{xx} & \epsilon'_{xy} & \epsilon'_{xz} \\ \epsilon'_{yx} & 1 + \epsilon'_{yy} & \epsilon'_{yz} \\ \epsilon'_{zx} & \epsilon'_{zy} & 1 + \epsilon'_{zz} \end{pmatrix}_d \mathbf{v}'_h \quad (15)$$

Combining the two steps, the lattice vectors transform following

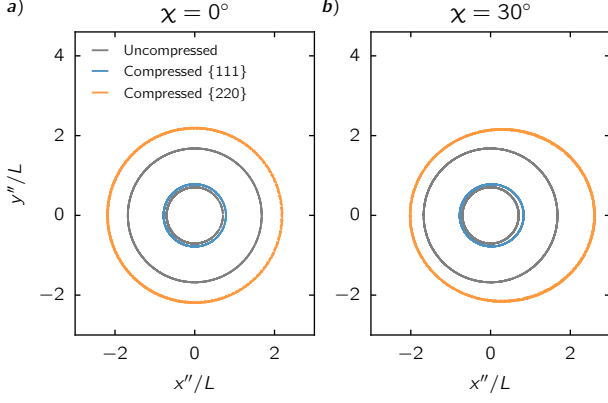


FIG. 2. (color) Debye-Scherrer diffraction patterns calculated for uniaxially compressed diamond with $\sigma_h = 200$ GPa and $t = 100$ GPa probed with a collimated 10 keV x-ray source a) aligned with the direction of compression ($\chi = 0^\circ$) and b) at 30° off-normal. When $\chi \neq 0^\circ$ the compression of the diffracting planes depends on ϕ and the diffraction pattern becomes asymmetric.

$$\mathbf{v}' = \frac{\rho_0}{\rho_h} (\mathbf{C}^{-1} \sigma'_d) \mathbf{v}'_0. \quad (16)$$

The direction of the probe vector in uniaxial compression experiments using a collimated x-ray source can be defined by a single parameter, χ , which is the angle between the direction of compression and the probe vector. In this case, the diffracted rays are transformed into the diffraction coordinate system by $\mathbf{k}'' = \mathbf{R}_y(-\chi) \cdot \mathbf{k}$.

Figure 2 shows examples of the diffraction patterns calculated for polycrystalline diamond with no texture under uniaxial compression with $\sigma_h = 200$ GPa and $t = 100$ GPa probed with a collimated 10 keV x-ray source a) aligned with the direction of compression ($\chi = 0^\circ$) and b) for $\chi = 30^\circ$. When $\chi \neq 0^\circ$ the compression of the diffracting planes depends on ϕ as a result of the distribution \mathbf{G} vector orientations satisfying the diffraction condition. The direction of \mathbf{G} is normal to the diffracting plane, and thus the compression of the plane is related to $\mathbf{G} \cdot \hat{z}$.

V. EXAMPLE: SHOCK COMPRESSED DIAMOND

Diamond has been the focus of a number of recent dynamic compression studies.^{11,13,20,21,32} We consider the case of polycrystalline diamond uniaxially compressed to $\sigma_h = 200$ GPa probed with a collimated 10 keV x-ray probe to illustrate how this analysis can be applied.

A. Coordinate transformation

First, the rotation matrix between the sample coordinate system and a crystallite with the vector $[hkl]'$ aligned along the z direction is calculated. This geometry and the orientations sampled are shown in Fig. 5. The rotation of the crystallite about this vector is given by the angle α , where we define $\alpha = 0$ when x' lies in the xz plane, fully constraining the coordinate system without loss of generality. Given these conditions the rotation angles between the two coordinate systems are

$$\beta = \cos^{-1} \left(\frac{l}{\sqrt{h^2 + k^2 + l^2}} \right) \quad (17)$$

$$\gamma = \cos^{-1} \left(\frac{h}{\sqrt{h^2 + k^2}} \right). \quad (18)$$

and α ranges from 0 to 2π radians.

B. Lattice strain calculations

Here we assume a sample compressed to a mean stress of 200 GPa shocked in the z direction. The applied stress tensor is given by

$$\sigma = \begin{pmatrix} 200 & 0 & 0 \\ 0 & 200 & 0 \\ 0 & 0 & 200 \end{pmatrix} \text{ GPa} + \begin{pmatrix} -t/3 & 0 & 0 \\ 0 & -t/3 & 0 \\ 0 & 0 & 2t/3 \end{pmatrix}, \quad (19)$$

where the uniaxial stress component, t , has been left as a variable to demonstrate how the deviatoric stress affects the diffraction pattern.

We assume the initial properties of polycrystalline diamond, $\rho_0 = 3.515$ g/cm³ and $a_0 = 3.56683$ Å. Following the method described for uniaxial compression, the hydrostatic component is applied, which gives the new lattice parameter of the cell. Using the hydrostatic DFT results shown in Fig. 3, the density is found to be 4.65 g/cm³, or a compression of 1.32, corresponding to a compressed lattice vector of $a = a_0(\rho_0/\rho)^{1/3} = 3.25$ Å.

Next, the deviatoric stress tensor is applied to the hydrostatically compressed diamond crystallites. The symmetry of cubic crystal systems reduces the number of independent elastic constants to three: C_{11} , C_{12} , and C_{44} . The stress-strain relationship is thus

$$\begin{pmatrix} \sigma'_{xx} \\ \sigma'_{yy} \\ \sigma'_{zz} \\ \tau'_{yz} \\ \tau'_{zx} \\ \tau'_{xy} \end{pmatrix} = \begin{pmatrix} C_{11} & C_{12} & C_{12} & 0 & 0 & 0 \\ C_{12} & C_{11} & C_{12} & 0 & 0 & 0 \\ C_{12} & C_{12} & C_{11} & 0 & 0 & 0 \\ 0 & 0 & 0 & C_{44} & 0 & 0 \\ 0 & 0 & 0 & 0 & C_{44} & 0 \\ 0 & 0 & 0 & 0 & 0 & C_{44} \end{pmatrix} \begin{pmatrix} \epsilon'_{xx} \\ \epsilon'_{yy} \\ \epsilon'_{zz} \\ \epsilon'_{yz} \\ \epsilon'_{zx} \\ \epsilon'_{xy} \end{pmatrix}. \quad (20)$$

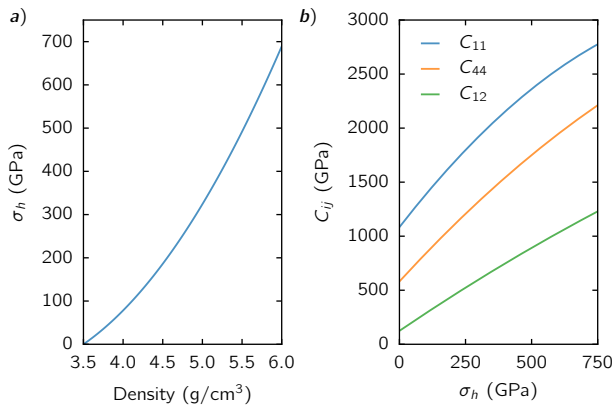


FIG. 3. (color) DFT calculations of the a) hydrostatic cold curve and b) elastic constants as a function of hydrostatic pressure for diamond.

The elastic constants from DFT as a function of hydrostatic pressure shown in Fig. 3 can then be used to calculate the lattice strains and compressed lattice vectors. Accounting for shearing, the strained cubic unit cell is a parallelepiped, with a volume given by $V = \mathbf{a}' \cdot \mathbf{b}' \times \mathbf{c}'$ and the compression of the unit cell for each initial orientation can be calculated using $\rho/\rho_0 = a_0^3/V$.

C. DFT calculations

The computation of the elastic constants of diamond at various hydrostatic pressures is performed using the DFT implementation as available in the package abinit.³³ We performed all calculations with a parallel implementation of abinit at the National Energy Research Scientific Computing Center (NERSC).³⁴ The results of these calculations are shown in Fig. 3.

The actual calculation of the elastic constants relies on a linear response formalism.³⁵ We have used norm-conserving Troullier-Martins type pseudopotentials from the Fritz-Haber-Institute (FHI) database with four electrons taken into account explicitly.³⁶ The electronic wave function was represented using plane waves with a cut-off of $E_{cut} = 35$ Ha. The self consistency loop for the electronic density was enforced to 10^{-18} in the residual of the potential and 10^{-20} in the wave function convergence, respectively. The exchange correlation potential was taken in PBE parametrization of the generalized gradient approximation.³⁷ Standard Monkhorst-Pack k-point sampling with $32 \times 32 \times 32$ k-points was invoked. The lattice constant was adjusted so as to give the desired hydrostatic pressure on the diamond unit cell consisting of two atoms (space group Fd3m) before invoking the response function calculation of the elastic constants.

For diamond at $\sigma_h = 200$ GPa the values calculated were $C_{11} = 1670$ GPa, $C_{12} = 446$ GPa, and $C_{44} = 1090$ GPa.

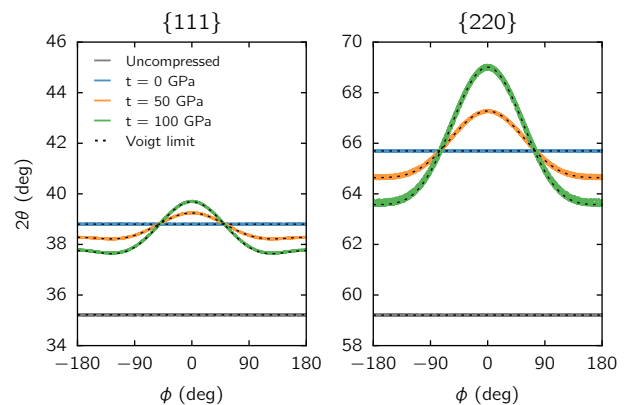


FIG. 4. (color) Diffraction calculations for polycrystalline diamond for $\sigma_h = 200$ GPa and $t = 0, 50$, and 100 GPa probed with 10 keV x-rays with $\chi = 30^\circ$. 2θ plotted as a function of ϕ for a) {111} and b) {220} diffraction. The width of the peaks in 2θ broadens with increasing t as a result of the distribution of strain states created by the increasingly anisotropic stress on the range of initial crystallite orientations, which is not present in the Voigt limit prediction (dashed).

D. Diffraction calculation

With the compressed lattice vectors defined, the diffraction pattern is calculated with t as a parameter. Figure 4 shows the calculated diffraction for diamond compressed to a hydrostatic pressure of 200 GPa and $t = 0, 50$, and 100 GPa. When $t = 0$ (hydrostatic compression) all crystallites are compressed identically, resulting in a single 2θ diffraction angle with no ϕ dependence. When t is nonzero the compression of the crystallites depends on initial orientation, creating a ϕ dependence and broadening diffraction in 2θ . This broadening is a result of the distribution of strain states created by the anisotropic stress applied to the polycrystalline sample. The Voigt limit prediction is shown for the strain tensor calculated for the unrotated stress tensor using the DFT results. The strains used in the Voigt calculations are $\epsilon_z = \epsilon_x = 0.937$ for $t = 0$ GPa, $\epsilon_z = 0.121$ and $\epsilon_x = 0.0805$ for $t = 50$ GPa, and $\epsilon_z = 0.148$ and $\epsilon_x = 0.0667$ for $t = 100$ GPa, where all strains are given in compression and it is assumed that the strains in the transverse directions are equal ($\epsilon_x = \epsilon_y$).

E. Texture effects

The texture of a polycrystalline material defines the distribution of crystallite orientations within the sample. Methods used to produce polycrystalline materials, such as chemical vapor deposition growth or rolling, often create characteristic textures. The properties of a crystalline material, such as strength and wave propagation, can be significantly affected by texture.³⁸

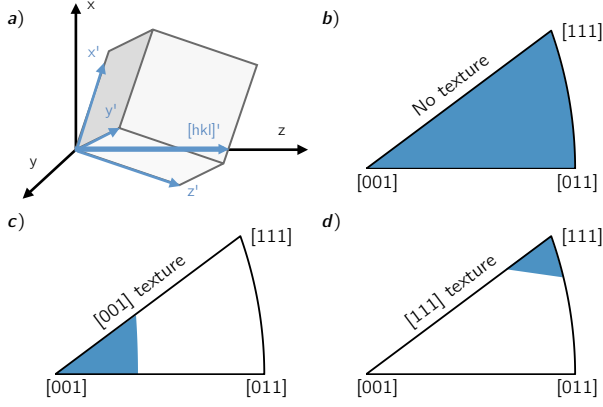


FIG. 5. (color) Crystallites with different initial orientations are sampled to calculate the diffraction from the polycrystalline sample. a) Each iteration calculates diffraction from a crystallite with lattice vector $[hkl]'$ aligned with z . Three texture cases were analyzed and their orientation distribution functions were represented by inverse pole figures. The three cases were: b) no texture, where all crystallite orientations are sampled equally, c) preferred [001] texture, and d) preferred [111] texture where the shaded regions represent the orientations included in each case.

Including texture in the prediction of diffraction from highly-strained polycrystalline materials has been explored in the Voigt limit.³⁹ Here we work in the Reuss limit, thereby including the effects of elastic anisotropy when calculating the response of each crystallite orientation within the sample. In doing so, we avoid having to measure or calculate the bulk and shear moduli for each texture case to accurately model the stress-strain relationship of the material. In this method the elastic constants are calculated only once and can be applied to any texture case.

Material texture can be characterized using an orientation distribution function (ODF), defining the probability distribution of crystallite orientations. In this method, the ODF is used to weight the scattering intensity from each initial crystallite orientation. We define crystallite orientation by the $[hkl]'$ vector aligned with the surface normal, z .

The cubic symmetry of diamond reduces the possible crystallite orientations to the projection into a space bound by [001], [011], and [111] directions. Figure 5 shows inverse pole figures illustrating the three example textures examined in this study: b) no texture, defined by a completely random distribution of crystallite orientations, c) a sample with [001] texture, and d) a sample with [111] texture where the shaded regions indicate the initial orientations present in each texture case. It should be noted that diffraction from the complete set of equivalent planes must be calculated when utilizing crystal symmetry to reduce the set of initial orientations. For example, diffraction from the $\{111\}$ family of planes in a cubic system must include diffraction from (111), ($\bar{1}\bar{1}$),

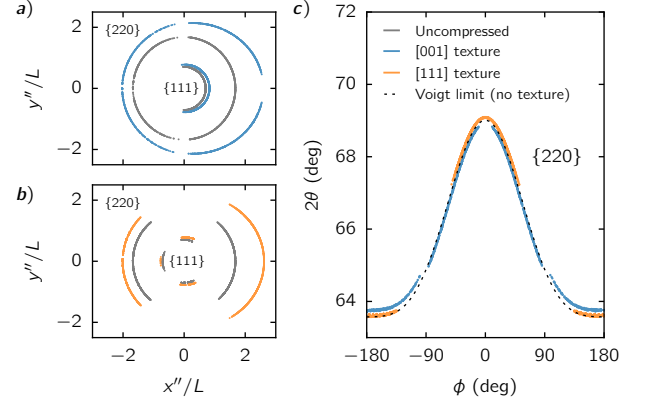


FIG. 6. (color) Diffraction patterns from $\{111\}$ and $\{220\}$ planes for polycrystalline diamond under uniaxial compression with $\sigma_h = 200$ GPa and $t = 100$ GPa probed with 10 keV x-rays at $\chi = 30^\circ$ shown in detector coordinates for a) [001] sample texture and b) [111] sample texture and c) $\{220\}$ diffraction plotted for both texture cases as a function of ϕ and the Voigt limit for the untextured case. The difference in 2θ for the two texture cases results from different final compression states for the initial textures.

($\bar{1}\bar{1}$), ($\bar{1}1$), etc.

Diffraction from 10 keV probe x-rays at $\chi = 30^\circ$ for each of these texture cases with $\sigma_h = 200$ GPa and $t = 100$ GPa is shown in Figure 6. Diffraction patterns are plotted in Cartesian coordinates for a) the [001] and b) [111] texture cases. These plots show gaps in the diffraction patterns, demonstrating the importance of knowing the initial texture of the sample when choosing detector locations. Diffraction from the $\{220\}$ planes is shown as a function of ϕ for each texture case as well as the Voigt limit for the untextured case, showing the differences in 2θ from the elastic anisotropy of diamond. The [111] texture case has a larger range of 2θ angles, suggesting that compressing diamond along the [111] direction creates a larger distribution of strains than when compressed along the [001] direction.

F. Strength calculations

Material strength is an important material property that can be studied using dynamic compression. The strength of a material describes its ability to support shear stresses and deviate from the hydrostat in response to an anisotropic stress. Using the von Mises yield criterion, the yield strength, σ_Y , and shear strength, τ_Y , are given by

$$\sigma_Y = 2\tau_Y = t. \quad (21)$$

If the stress tensor applied to a material can be determined using time resolved x-ray diffraction the strength is obtained by calculating t in Eq. (12).

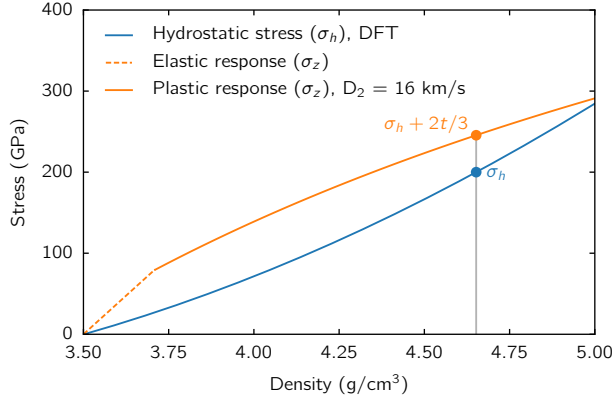


FIG. 7. (color) Pressure-density relationships for hydrostatically compressed diamond, calculated using DFT (blue) and planar shock Hugoniot calculations using Eq. (22) for an elastic precursor with $D_1 = 20$ km/s and $\sigma_{z1} = 80$ GPa and a plastic deformation wave with $D_2 = 16$ km/s (orange). For a given material density, σ_h and t are known and the stress tensor for uniaxial compression defined by Eq. (12) is fully defined.

Here we consider a shock compression experiment where the time-resolved x-ray diffraction from the $\{111\}$ planes and the plastic deformation wave velocity are measured. If the conditions of the elastic precursor are known (pressure and shock velocity), the Rankine-Hugoniot shock conditions can be used to calculate the post-shock stress of the plastic wave in the shock direction as a function of plastic wave velocity⁴⁰

$$\sigma_{z2} = \rho_0 D_1 u_1 + \rho_1 (D_2 - u_1) (u_2 - u_1) \quad (22)$$

where σ is stress, ρ is density, D is shock velocity, and u is particle velocity, and the subscripts 0, 1, and 2 denote the unshocked material, elastic precursor, and plastic deformation wave, respectively. Here we have specified the stress in the shock (z) direction because the shocked material is not under hydrostatic compression and stresses in the orthogonal plane are not governed by this equation. The particle velocities are given by

$$u_1 = D_1 \left(1 - \frac{\rho_0}{\rho_1} \right) \quad (23)$$

$$u_2 = D_2 \left(1 - \frac{\rho_1}{\rho_2} \right) + D_1 \left(\frac{\rho_1 - \rho_0}{\rho_2} \right). \quad (24)$$

These equations define the pressure in the shock direction as a function of densities and shock velocities. The pressure-density curve is plotted in Fig. 7 for a plastic wave velocity of 16 km/s with elastic precursor conditions of $D_1 = 20$ km/s and $\sigma_{z1} = 80$ GPa, which have been previously measured in shock-compressed diamond.¹³ The

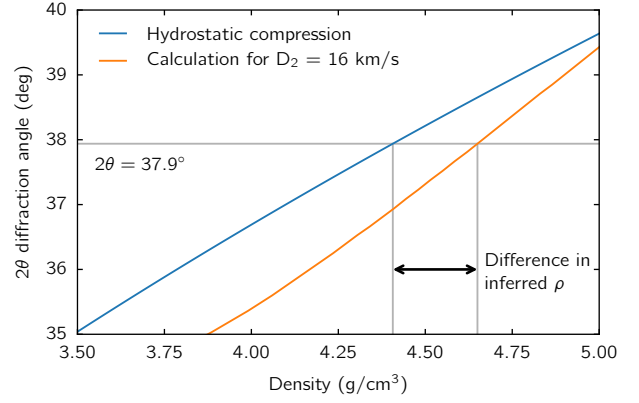


FIG. 8. (color) Calculated $\{111\}$ diffraction from polycrystalline diamond probed at 10 keV and $\chi = 0$ under hydrostatic compression (blue) and mean 2θ diffraction angles calculated for a plastic deformation wave velocity of $D_2 = 16$ km/s and an elastic precursor with $D_1 = 20$ km/s and $\sigma_{z1} = 80$ GPa (orange). The difference in inferred density for a measured 2θ of 37.9° with and without strength is illustrated.

dashed line shows the elastic response of diamond and the solid line is defined by Eq (22).

The hydrostatic behavior of diamond calculated using DFT is shown in Fig. 7 by the solid blue line. The hydrostatic response gives σ_h and Eq. (22) defines the stress in the shock direction, which is $\sigma_h + 2t/3$. These two stress values fully define the stress tensor in the laboratory frame given by Eq. (12) as a function of material density.

For simplicity, we consider the case of normal probe incidence ($\chi = 0$), where 2θ has no ϕ dependence. The mean 2θ diffraction angle for each density and is shown in Fig. 8. If the probe is not normal to the drive surface ($\chi \neq 0$) the strength can be inferred by the ϕ dependence on 2θ , as illustrated in Fig. 4.

The measured 2θ diffraction peak from the $\{111\}$ planes can be compared to Fig. 8 and the material density can be inferred. The difference in density inferred with strength compared to hydrostatic compression can be rather large as illustrated by the example of a measured 2θ of 37.9° , resulting in a 5.5% difference in density. The stress tensor applied to produce the inferred density state is known from Fig. 7 and the yield strength and distribution of lattice strains can be calculated for the applied stress tensor. In this example we calculate the yield strength to be $\sigma_Y = t = 68$ GPa and $\sigma_h = 200$ GPa.

VI. CONCLUSION

We have presented a method to calculate Debye-Scherrer diffraction patterns from highly stressed polycrystalline materials. Example diffraction patterns for cases with different probe geometries, deviatoric stresses,

and initial sample textures illustrate the robust nature of this method. Comparisons to the Voigt limit show where the Voigt and Reuss limits differ and the validity of these models could be tested. By working in the Reuss limit and applying stresses to all initial crystallite orientations, peak widths resulting from elastic anisotropy can be calculated. Additionally, the Reuss limit allows pressure measurements and equation-of-state models to be compared directly to diffraction measurements. This flexible analysis enables diffraction from materials with any texture and a wide variety of stress conditions to be modeled within the Reuss limit.

We have shown how this method can be applied to the case of polycrystalline diamond under uniaxial compression. Using the elastic constants calculated with DFT and shock Hugoniot equations, we demonstrated how this analysis can be applied to calculate strength from diffraction measurements when a limited number of diffraction

lines are available. These results illustrate how strength can have a significant impact on material density inferred from diffraction measurements.

ACKNOWLEDGMENTS

This material is based upon work supported by the National Science Foundation Graduate Research Fellowship Program under Grant No. 2013155705. This work was supported by DOE Office of Science, Fusion Energy Science under FWP 100182. This work is funded by the NNSA-DS and SC-OFES Joint Program in High-Energy-Density Laboratory Plasmas, grant number DE-NA0002956. This research used resources of the National Energy Research Scientific Computing Center, a DOE Office of Science User Facility supported by the Office of Science of the U.S. Department of Energy under Contract No. DE-AC02-05CH11231.

* macdonm@umich.edu

¹ T. Guillot, *Science* **286**, 72 (1999).

² F. Coppari, R. F. Smith, J. H. Eggert, J. Wang, J. R. Rygg, A. Lazicki, J. A. Hawreliak, G. W. Collins, and T. S. Duffy, *Nature Geosci* **6**, 926 (2013).

³ A. E. Gleason, C. A. Bolme, H. J. Lee, B. Nagler, E. Galtier, D. Milathianaki, J. Hawreliak, R. G. Kraus, J. H. Eggert, D. E. Fratanduono, G. W. Collins, R. Sandberg, W. Yang, and W. L. Mao, *Nat Commun* **6** (2015).

⁴ D. Kraus, A. Ravasio, M. Gauthier, D. Gericke, J. Vorberger, S. Frydrych, J. Helfrich, L. Fletcher, G. Schumann, B. Nagler, B. Barbrel, B. Bachmann, E. Gamboa, S. Goede, E. Granados, G. Gregori, H. Lee, P. Neumayer, W. Schumaker, T. Doeppner, R. Falcone, S. Glenzer, and M. Roth, *Nature Communications* (accepted for publication, 2016).

⁵ J. D. Lindl, P. Amendt, R. L. Berger, S. G. Glendinning, S. H. Glenzer, S. W. Haan, R. L. Kauffman, O. L. Landen, and L. J. Suter, *Physics of Plasmas* **11**, 339 (2004).

⁶ A. J. MacKinnon, N. B. Meezan, J. S. Ross, S. Le Pape, L. Berzak Hopkins, L. Divol, D. Ho, J. Milovich, A. Pak, J. Ralph, T. Döppner, P. K. Patel, C. Thomas, R. Tomasini, S. Haan, A. G. MacPhee, J. McNaney, J. Caggiano, R. Hatarik, R. Bionta, T. Ma, B. Spears, J. R. Rygg, L. R. Benedetti, R. P. J. Town, D. K. Bradley, E. L. Dewald, D. Fittinghoff, O. S. Jones, H. R. Robey, J. D. Moody, S. Khan, D. A. Callahan, A. Hamza, J. Biener, P. M. Celliers, D. G. Braun, D. J. Erskine, S. T. Prisbrey, R. J. Wallace, B. Kozioziemski, R. Dylla-Spears, J. Sater, G. Collins, E. Storm, W. Hsing, O. Landen, J. L. Atherton, J. D. Lindl, M. J. Edwards, J. A. Frenje, M. Gatu-Johnson, C. K. Li, R. Petrasso, H. Rinderknecht, M. Rosenberg, F. H. Séguin, A. Zylstra, J. P. Knauer, G. Grim, N. Guler, F. Merrill, R. Olson, G. A. Kyrala, J. D. Kilkenny, A. Nikroo, K. Moreno, D. E. Hoover, C. Wild, and E. Werner, *Physics of Plasmas* **21**, 056318 (2014).

⁷ M. Gauthier, L. B. Fletcher, A. Ravasio, E. Galtier, E. J.

Gamboa, E. Granados, J. B. Hastings, P. Heimann, H. J. Lee, B. Nagler, A. Schropp, A. Gleason, T. Döppner, S. LePape, T. Ma, A. Pak, M. J. MacDonald, S. Ali, B. Barbrel, R. Falcone, D. Kraus, Z. Chen, M. Mo, M. Wei, and S. H. Glenzer, , 11.

⁸ L. B. Fletcher, H. J. Lee, T. Döppner, E. Galtier, B. Nagler, P. Heimann, C. Fortmann, S. LePape, T. Ma, M. Milot, A. Pak, D. Turnbull, D. A. Chapman, D. O. Gericke, J. Vorberger, T. White, G. Gregori, M. Wei, B. Barbrel, R. W. Falcone, C. C. Kao, H. Nuhn, J. Welch, U. Zastrau, P. Neumayer, J. B. Hastings, and S. H. Glenzer, *Nat Photon* **9**, 274 (2015).

⁹ J. S. Wark, R. R. Whitlock, A. Hauer, J. E. Swain, and P. J. Solone, *Phys. Rev. B* **35**, 9391 (1987).

¹⁰ J. S. Wark, R. R. Whitlock, A. A. Hauer, J. E. Swain, and P. J. Solone, *Phys. Rev. B* **40**, 5705 (1989).

¹¹ M. D. Knudson, M. P. Desjarlais, and D. H. Dolan, *Science* **322**, 1822 (2008).

¹² J. H. Eggert, D. G. Hicks, P. M. Celliers, D. K. Bradley, R. S. McWilliams, R. Jeanloz, J. E. Miller, T. R. Boehly, and G. W. Collins, *Nat Phys* **6**, 40 (2010).

¹³ R. S. McWilliams, J. H. Eggert, D. G. Hicks, D. K. Bradley, P. M. Celliers, D. K. Spaulding, T. R. Boehly, G. W. Collins, and R. Jeanloz, *Phys. Rev. B* **81**, 014111 (2010).

¹⁴ W. J. Murphy, A. Higginbotham, G. Kimminau, B. Barbrel, E. M. Bringa, J. Hawreliak, R. Kodama, M. Koenig, W. McBarron, M. A. Meyers, B. Nagler, N. Ozaki, N. Park, B. Remington, S. Rothman, S. M. Vinko, T. Whitcher, and J. S. Wark, *Journal of Physics: Condensed Matter* **22**, 065404 (2010).

¹⁵ S. J. Turneare and Y. M. Gupta, *Journal of Applied Physics* **109**, 123510 (2011).

¹⁶ J. A. Hawreliak, B. El-Dasher, H. Lorenzana, G. Kimminau, A. Higginbotham, B. Nagler, S. M. Vinko, W. J. Murphy, T. Whitcher, J. S. Wark, S. Rothman, and N. Park, *Phys. Rev. B* **83**, 144114 (2011).

¹⁷ V. H. Whitley, S. D. McGrane, D. E. Eakins, C. A. Bolme, D. S. Moore, and J. F. Bingert, *Journal of Applied Physics*

- 109**, 013505 (2011).
- ¹⁸ D. Milathianaki, S. Boutet, G. J. Williams, A. Higginbotham, D. Ratner, A. E. Gleason, M. Messerschmidt, M. M. Seibert, D. C. Swift, P. Hering, J. Robinson, W. E. White, and J. S. Wark, *Science* **342**, 220 (2013).
 - ¹⁹ C. E. Wehrenberg, A. J. Comley, N. R. Barton, F. Coppari, D. Fratanduono, C. M. Huntington, B. R. Maddox, H.-S. Park, C. Plechaty, S. T. Prisbrey, B. A. Remington, and R. E. Rudd, *Phys. Rev. B* **92**, 104305 (2015).
 - ²⁰ D. K. Bradley, J. H. Eggert, R. F. Smith, S. T. Prisbrey, D. G. Hicks, D. G. Braun, J. Biener, A. V. Hamza, R. E. Rudd, and G. W. Collins, *Phys. Rev. Lett.* **102**, 075503 (2009).
 - ²¹ R. F. Smith, J. H. Eggert, R. Jeanloz, T. S. Duffy, D. G. Braun, J. R. Patterson, R. E. Rudd, J. Biener, A. E. Lazicki, A. V. Hamza, J. Wang, T. Braun, L. X. Benedict, P. M. Celliers, and G. W. Collins, *Nature* **511**, 330 (2014).
 - ²² A. Lazicki, J. R. Rygg, F. Coppari, R. Smith, D. Fratanduono, R. G. Kraus, G. W. Collins, R. Briggs, D. G. Braun, D. C. Swift, and J. H. Eggert, *Phys. Rev. Lett.* **115**, 075502 (2015).
 - ²³ C. A. Hall, *Physics of Plasmas* **7** (2000).
 - ²⁴ C. A. Hall, J. R. Asay, M. D. Knudson, W. A. Stygar, R. B. Spielman, T. D. Pointon, D. B. Reisman, A. Toor, and R. C. Cauble, *Review of Scientific Instruments* **72** (2001).
 - ²⁵ D. B. Reisman, A. Toor, R. C. Cauble, C. A. Hall, J. R. Asay, M. D. Knudson, and M. D. Furnish, *Journal of Applied Physics* **89** (2001).
 - ²⁶ J. Edwards, K. T. Lorenz, B. A. Remington, S. Pollaine, J. Colvin, D. Braun, B. F. Lasinski, D. Reisman, J. M. McNaney, J. A. Greenough, R. Wallace, H. Louis, and D. Kalantar, *Phys. Rev. Lett.* **92**, 075002 (2004).
 - ²⁷ H.-S. Park, N. Barton, J. L. Belof, K. J. M. Blobaum, R. M. Cavallo, A. J. Comley, B. Maddox, M. J. May, S. M. Pollaine, S. T. Prisbrey, B. Remington, R. E. Rudd, D. W. Swift, R. J. Wallace, M. J. Wilson, A. Nikroo, and E. Giraldez, *AIP Conference Proceedings* **1426** (2012).
 - ²⁸ W. Voigt, *Lehrbuch der kristallphysik* (Leipzig, Berlin, B.G. Teubner, 1928).
 - ²⁹ A. Reuss, *Journal of Applied Mathematics and Mechanics* **9**, 49 (1929).
 - ³⁰ A. K. Singh, *Journal of Applied Physics* **73**, 4278 (1993).
 - ³¹ A. Higginbotham and D. McGonegle, *Journal of Applied Physics* **115**, 174906 (2014).
 - ³² K.-i. Kondo and T. J. Ahrens, *Geophysical Research Letters* **10**, 281 (1983).
 - ³³ X. Gonze, B. Amadon, P.-M. Anglade, J.-M. Beuken, F. Bottin, P. Boulanger, F. Bruneval, D. Caliste, R. Caracas, M. Ct, T. Deutsch, L. Genovese, P. Ghosez, M. Giantomassi, S. Goedecker, D. Hamann, P. Hermet, F. Jollet, G. Jomard, S. Leroux, M. Mancini, S. Mazevet, M. Oliveira, G. Onida, Y. Pouillon, T. Rangel, G.-M. Rignanese, D. Sangalli, R. Shaltaf, M. Torrent, M. Verstraete, G. Zerah, and J. Zwanziger, *Computer Physics Communications* **180**, 2582 (2009), 40 {YEARS} {OF} CPC: A celebratory issue focused on quality software for high performance, grid and novel computing architectures.
 - ³⁴ F. Bottin, S. Leroux, A. Knyazev, and G. Zerah, *Computational Materials Science* **42**, 329 (2008).
 - ³⁵ D. R. Hamann, X. Wu, K. M. Rabe, and D. Vanderbilt, *Phys. Rev. B* **71**, 035117 (2005).
 - ³⁶ M. Fuchs and M. Scheffler, *Computer Physics Communications* **119**, 67 (1999).
 - ³⁷ J. P. Perdew, K. Burke, and M. Ernzerhof, *Phys. Rev. Lett.* **77**, 3865 (1996).
 - ³⁸ H.-R. Wenk and P. V. Houtte, *Reports on Progress in Physics* **67**, 1367 (2004).
 - ³⁹ D. McGonegle, D. Milathianaki, B. A. Remington, J. S. Wark, and A. Higginbotham, *Journal of Applied Physics* **118**, 065902 (2015).
 - ⁴⁰ R. P. Drake, *High-Energy-Density Physics*, edited by L. Davison and Y. Horie, *Shock Wave and High Pressure Phenomena* (Springer Berlin Heidelberg, 2006).